Materials Science & Engineering A 820 (2021) 141420

Contents lists available at ScienceDirect

Materials Science & Engineering A

journal homepage: www.elsevier.com/locate/msea

Effects of constituent particle content on ductile fracture in isotropic and anisotropic 6000-series aluminium alloys

Asle Joachim Tomstad [a,*], Susanne Thomesen [a,b], Tore Børvik [a,b], Odd Sture Hopperstad [a,b]

[a] Structural Impact Laboratory (SIMLab), Department of Structural Engineering, NTNU - Norwegian University of Science and Technology, Trondheim, Norway
[b] Centre for Advanced Structural Analysis (CASA), NTNU, Trondheim, Norway

ARTICLE INFO

Keywords:
Aluminium
Ductility
Fracture
Constituent particles
Tensile tests

ABSTRACT

Tension tests on smooth and notched specimens were conducted for four 6000-series aluminium alloys to assess the effects of constituent particles on ductile fracture at different stress states. Two of the alloys are engineering materials, while the remaining two were tailor-made to be similar to the engineering materials but with more than three times the amount of constituent particles. The microstructure of both isotropic (cast and homogenised) and anisotropic (extruded) materials was characterised using scanning electron microscopy (SEM), optical microscopy and X-ray diffraction. Axisymmetric smooth and notched specimens were machined from cast and homogenised billets and extruded profiles. All specimens were tested in the artificially aged T6 temper. The specimens were strained in tension until fracture, and the fracture surface of the specimens was later investigated based on SEM images. The experiments show that the ductility is significantly improved by extrusion, while a high stress triaxiality and a high volume fraction of large-sized constituent particles have a detrimental effect on the ductility. However, the negative effect of the increased particle volume fraction on ductility was markedly reduced after extrusion. The experiments also indicated that a larger amount of constituent particles may improve the ductility under certain conditions.

1. Introduction

Aluminium alloys have found many applications as engineering materials owing to their high strength-to-weight ratio, good formability and excellent corrosion resistance. Transportation and construction are typical sectors where the application of aluminium is well suited and environmentally friendly. In the automotive industry, components made of aluminium alloys are highly efficient as crash absorbers, and the application of aluminium for weight reduction improves the fuel efficiency. The global demand of aluminium is high, and it is expected to increase by 50% within year 2050, which means that recycling is required to reach the emission reduction goals [1]. Aluminium recycling is not without problems, as the amount of silicon (Si) and iron (Fe) accumulates during recycling [2], and these alloying elements are a known source of constituent particles due to their low solubility in aluminium [3]. A larger amount of constituent particles may reduce the ductility, as the constituent particles act as nucleation sites for microvoids.

Ductile fracture occurs by nucleation, growth and coalescence of microvoids, see e.g. Refs. [4,5]. Nucleation of microvoids at constituent particles has been observed to occur by several mechanisms. Beremin [6] identified voids which nucleated by cracking of the constituent particles and also by decohesion between the constituent particles and the matrix material. The former was also reported by Frodal et al. [7]. Microvoids have in addition been observed prior to deformation by Toda et al. [8] in the form of hydrogen filled pores in the vicinity of constituent particles. Experiments conducted by Babout et al. [9] showed that the nucleation mechanism may be influenced by the hardness of the matrix material. Several authors, such as Beremin [6], Lassance et al. [10], Achouri et al. [11] and Agarwal et al. [12,13], have experimentally shown that the stress state may influence the nucleation mechanism. Beremin [6], Agarwal et al. [12], and Gurland and Plateau [14] address the effect of the loading direction relative to the orientation of the constituent particle upon void nucleation, and conclude that there is a correlation.

Void growth is governed by plastic straining, and several studies have found that parameters such as the stress triaxiality accelerate the void growth, see e.g., Agarwal et al. [13], Weck et al. [15] and Benzerga et al. [16]. Experiments conducted by Benzerga et al. [16] revealed anisotropic void growth rates, and the authors attributed this effect to the anisotropic plastic flow of the matrix material. The distortion of

* Corresponding author.
E-mail address: asle.j.tomstad@ntnu.no (A.J. Tomstad).

https://doi.org/10.1016/j.msea.2021.141420
Received 24 February 2021; Received in revised form 29 April 2021; Accepted 1 May 2021
Available online 13 May 2021

voids, which usually occurs at lower triaxialities, has been observed by Achouri et al. [11]. In some cases, the constituent particle has been found to constrain the void deformation. This phenomenon is known as void locking and has been found in experiments conducted by Babout et al. [9] and Benzerga et al. [16].

Several void coalescence mechanisms have been distinguished experimentally. Benzerga et al. [16] document necklace coalescence, which typically occurs at lower stress triaxialities. Coalescence of voids by necking of the inter-void ligament is also reported by Benzerga et al. [16] and Weck et al. [17]. Micro-shearing between voids has been observed as a coalescence mechanism in several studies, e.g. Cox and Low [18] and Weck and Wilkinson [19]. Experiments performed by Weck et al. [17] and Weck and Wilkinson [19] suggest that the occurrence of these coalescence mechanisms depends upon the void spacing, the orientation of the voids relative to the loading direction, and the nucleation of secondary voids. Hannard et al. [20] link anisotropy in the failure strain to the spatial distribution of clusters and to inter-cluster coalescence. Kondori et al. [21] substantiate this notion and further observe that coalescence may occur in certain directions before others due to the heterogeneous distribution of constituent particles.

By tailoring materials, certain aspects of the mechanisms involved in ductile fracture may be isolated and their significance on chosen metrics assessed. Tailor-made materials, or model materials, are not new within ductility research. For example, Babout et al. [9] embedded spherical particles into two different aluminium matrix materials by using powder metallurgy to assess the void nucleation mechanisms. In a similar fashion, Weck et al. [15] used powder metallurgy to create composite axisymmetric specimens with different amounts of large spherical particles in the inner core to study the effect of stress triaxiality on void growth. Lassance et al. [10] altered the temperature and time of the homogenisation procedure to investigate the detrimental effects of β-particles on the fracture strain, whereas Kato et al. [22] and Remøe et al. [23] used aluminium alloys cast in research laboratories to assess the effect of different alloying elements on ductility. Hannard et al. [24] utilised friction stir welding to break up and rearrange particles to investigate the effect of clustering. By considering aluminium alloys with three different heat treatments, Frodal et al. [7] investigated the effect of work hardening on ductile fracture under reversed loading conditions. In Frodal et al. [25], the effect of quench rate after solution heat treatment on the plastic flow and fracture of three artificially aged aluminium alloys with different grain structure and texture was studied.

In this study, we use two of the engineering alloys studied by Thomesen et al. [26] as a basis for two new tailor-made alloys which contain a much larger amount of constituent particles while maintaining the same matrix material as the base alloys. Since the strength and work hardening properties are similar for the tailor-made alloy and the corresponding engineering alloy, the effect of the higher constituent particle content on ductility can be investigated. The two tailor-made alloys are compared to the engineering alloys with respect to microstructure, macroscopic stress-strain response, ductility and fracture behaviour. All four alloys are studied in the cast and homogenised condition as well as in the extruded condition. The material characterisation prior to and after extrusion revealed that the matrix material of the tailor-made alloys closely resembles that of their respective engineering alloy, while their constituent particle content was successfully increased. The particle characterisation shows changes in the constituent particle size and spatial distribution after extrusion for all four alloys. There is a clear detrimental effect of a larger constituent particle population on ductility, but after extrusion this effect is reduced as the constituent particles are broken up and redistributed.

2. Materials and methods

2.1. Aluminium alloys

Four 6000-series aluminium alloys are considered of which two are engineering alloys and two are tailor-made. The engineering alloys AA6063 and AA6110 were used as the basis for the tailor-made alloys, where iron (Fe) and silicon (Si) were added to increase the amount of constituent particles formed during solidification. When increasing the amount of Fe to increase the volume fraction of constituent particles, it is important to also increase the Si level to retain the same level of Si in solid solution in the tailor-made alloy as in the engineering alloy after the solution heat treatment. This is because some Si will be tied up in the constituent particles. If this is not done, the strength and work hardening of the engineering and tailor-made alloy would be markedly different due to variations in the amounts of hardening precipitates and elements in solid solution, which could influence the ductility of the alloys [23, 27].

The plastic flow and fracture of the two engineering alloys were previously investigated in the cast and homogenised condition by Thomesen et al. [26] and in the extruded condition by Thomesen et al. [28]. The thermo-mechanical processing and the characterisation of the microstructure of the engineering alloys are described in detail in these studies, and the reader is referred there for further details. Even if the tailor-made alloys were processed similarly as the engineering alloys, some variation in their mechanical behaviour must be expected. A brief description of the procedures is therefore given in the following sections for completeness.

The chemical composition of the four alloys is presented in Table 1. Here, the label “A” represents the engineering alloys, while “B” denotes the alloys with an increased amount of Fe and Si. Table 1 shows that there are small differences in the content of various alloying elements besides Fe and Si in the A- and B-variants of an alloy, but these are considered minor.

The alloys were provided by Hydro R&D Sunndal and received as DC-cast billets with a 95 mm diameter. The billets were homogenised according to industrial standards at Hydro’s production facility, where they were heated to 575 °C with a heating rate of 200 °C/h and held at 575 °C for 135 min before cooled to room temperature with a rate of −400 °C/h. The further treatment of the billets was dependent on whether the alloy was to be tested in the cast and homogenised (CH) or the extruded (EX) condition.

Tensile test specimens of the four cast and homogenised alloys were machined from the billets prior to heat treatment. Thereafter, a solution heat treatment was applied to the specimens by heating them to 560 °C and holding for 10 min in a salt bath, before water quenching and storage at room temperature for 24 h. Lastly, the specimens were heated to 185 °C with a rate of 200 °C/h in a hot air circulation oven and kept at 185 °C for 8 h before water quenched to achieve temper T6.

Billets of the four alloys were extruded using a vertical extrusion press at SINTEF Industry into 40 mm wide and 6 mm thick profiles. Prior to extrusion, the homogenised billets were solution heat treated at 560 °C for 10 min, cooled to 500 °C and mounted in the extrusion press. Water quenching of the extruded profiles was provided 0.5 m below the press mold. After extrusion, the profiles were stretched 0.5% and stored at room temperature for 48 h. The profiles were then artificially aged to temper T6 by heating to 185 °C and holding for 8 h, before air cooling to room temperature. Tensile test specimens of the four extruded alloys were machined from the profiles after heat treatment. More details about the extrusion process can be found in the supplementary material of Thomesen et al. [28].

2.2. Microstructure characterisation

2.2.1. Cast and homogenised condition

The grain size of the cast and homogenised alloys was characterised using optical microscopy and the line intercept technique, while the constituent particles were measured and counted by analysing images captured by a scanning electron microscope (SEM). The latter technique requires a grey scale threshold value to be determined by the analyst, and this threshold value influences whether the pixels are counted as

Table 1
Chemical composition of the aluminium alloys in wt-%.

Alloy	Mg	Si	Fe	Cu	Mn	Zn	Ti	Cr	Al
6063A	0.470	0.512	0.206	0.001	0.047	0.003	0.006	0.001	Bal.
6063B	0.481	0.692	0.753	0.001	0.048	0.004	0.015	0.005	Bal.
6110A	0.828	0.720	0.196	0.203	0.506	0.003	0.026	0.157	Bal.
6110B	0.793	0.925	0.749	0.204	0.503	0.005	0.029	0.183	Bal.

particle or matrix. In the particle characterisation, the total area measured was 0.227 mm^2 for the A-variants and 0.399 mm^2 for the B-variants of the alloys. The threshold value was defined in terms of the equivalent particle diameter D_{eq}, which equals the diameter of a circular particle with the same area as the measured particle. To exclude dispersoids and noise, the threshold value for counting a constituent particle was taken as $D_{eq} > 0.2$ μm. The constituent particles were divided into size dependent groups, with a bin size of 25 μm. The area fraction of each group was calculated to obtain particle size distribution (PSD) of the respective material.

Pair correlation function (PCF) analyses of the constituent particles were conducted using a technique described in the supplementary material of Hannard et al. [20], which is an adaptation of a method originally proposed by Marthinsen et al. [29]. In brief, the PCFs are computed by placing a 20 μm × 20 μm square box in the centre of each constituent particle, and all pixels belonging to neighbouring constituent particles are logged. The boxes are summed and normalised with respect to the respective particle area fraction. The intensity, i.e., occurrence divided by global particle content, is plotted from 0 to 4 for comparison purposes.

2.2.2. Extruded condition

Images of the grain structure were obtained in an optical microscope, while the grain dimensions were measured by use of the line intercept technique on images created from electron backscatter diffraction (EBSD) measurements. Grain dimensions are provided in the TD-ND plane and in the ED-ND plane, where ED, TD and ND denote the extrusion, transverse and normal directions of the extruded profile, respectively. The constituent particles were characterised using an SEM, with a measured area of 0.235 mm^2 for the A-variants and 0.157 mm^2 for the B-variants of the extruded alloys. Both the PSDs and the PCFs were computed using the same method as for the cast and homogenised alloys, see description in Section 2.2.1. The characterisation of the constituent particles was conducted both in the TD-ND plane and the ED-ND plane.

To measure the global texture of the extruded alloys, the X-ray diffraction (XRD) method was used. The data were extracted as pole figures, and orientation distribution functions (ODFs) were subsequently reconstructed from the pole figures by using a harmonic series expansion and orthotropic sample symmetry with a series rank of 23 and Gaussian smoothing of 7° [30].

2.3. Mechanical test programme

The results from several mechanical test series are presented in this work. The test series for the A-variants of the cast and homogenised alloys and the extruded alloys were parts of previous studies and the results can also be found in Thomesen et al. [26] and Thomesen et al. [28], respectively. However, new test series were carried out for the tailor-made B-variants of these alloys. Results from all test series are presented here to investigate the influence of the higher amount of constituent particles on the tensile ductility.

All test series comprised tensile tests with smooth and notched axisymmetric specimens. Henceforth, we will denote tensile tests on smooth specimens for “uniaxial tension tests”, and tensile tests on notched specimens for “notch tension tests”. The cast and homogenised alloys were assumed to be isotropic, while the observed crystallographic texture of the extruded alloys revealed that they are anisotropic. Triplicate tests of each combination of alloy, condition and specimen type were conducted, except in some few cases for the extruded alloys where only duplicate tests were completed successfully.

The various specimens were tested in a universal testing machine with a constant crossbar velocity to ensure quasi-static conditions. The crossbar velocity was determined based on the specimen geometry and set to give an initial strain rate of $5 \times 10^{-4}\ s^{-1}$ for the smooth specimens. The force was measured directly from the load cell of the machine, while two perpendicular minimum cross-sectional diameters were continuously measured and recorded during testing using a laser gauge [31].

The axisymmetric smooth and notched tensile specimens presented in Fig. 1 were used for the cast and homogenised alloys. The smooth tensile specimen was tested at a constant crossbar velocity of 1 mm/min, while for the two notched tensile specimens, a velocity of 0.15 mm/min was used. Note that the notched specimens used for the A-variants of the two alloys had an outer diameter of 9.47 mm between the threaded section and the notch instead of the nominal value of 10 mm as shown in Fig. 1, see Thomesen et al. [26] for details. This resulted in a minor reduction in the triaxiality of the stress field in the notch region, which should be kept in mind when comparing the ductility of the A- and B-variants of the alloys obtained for the notched specimens.

Fig. 2 displays the axisymmetric smooth and notched tensile specimens used for the extruded alloys. Owing to the dimensions of the extruded profile, the size of these specimens had to be reduced compared with those used for the cast and homogenised alloys. It was shown in Thomesen et al. [32] that the shape and size of the specimen did not have any significant effect on the stress-strain response of these aluminium alloys in the cast and homogenised condition. Note that the radius of the notch does not scale and thus the triaxiality of the stress field within the notch region will not be the same as for the larger notched specimens used for the cast and homogenised alloys. However, as the aim of the current study is to evaluate the effect of an increased volume fraction of constituent particles, this is not considered to be an issue. The B-variants of the extruded alloys were tested in two directions, i.e., the 0° direction (tensile axis along the ED) and the 90° direction (tensile axis along the TD). Five directions were tested for the A-variants (i.e., 0°, 22.5°, 45°, 67.5°, 90° with respect to the extrusion direction), but only results from tests along ED and TD will be presented here. The smooth specimens were tested with a constant crossbar velocity of 0.15 mm/min, while 0.1 mm/min was applied for the notched specimens.

The minimum cross-sectional area was assumed to be elliptical when analysing the experimental results from the tensile tests. The current area is calculated as $A = \frac{\pi}{4} D_1 D_2$, where D_1 and D_2 are the two minimum cross-sectional diameters measured by the laser gauge. For the tensile tests on the extruded alloys, D_1 always corresponded to the diameter in the ND, while D_2 corresponded to the diameter in the TD and ED for the tests in the 0° and 90° direction, respectively. The true stress is given by $\sigma = F/A$, where F is the measured force. The materials are assumed to be isochoric, and therefore the logarithmic strain is calculated as $\varepsilon = \ln(A_0/A)$, where $A_0 = \frac{\pi}{4} D_0^2$ is the initial minimum cross-sectional area of the specimen and D_0 is the initial cross-section diameter. For the notched specimens and the smooth specimens after necking, the calculated true stress and logarithmic strain represent average values over the minimum cross-section. The failure strain ε_f is defined as the logarithmic strain corresponding to the maximum true stress.

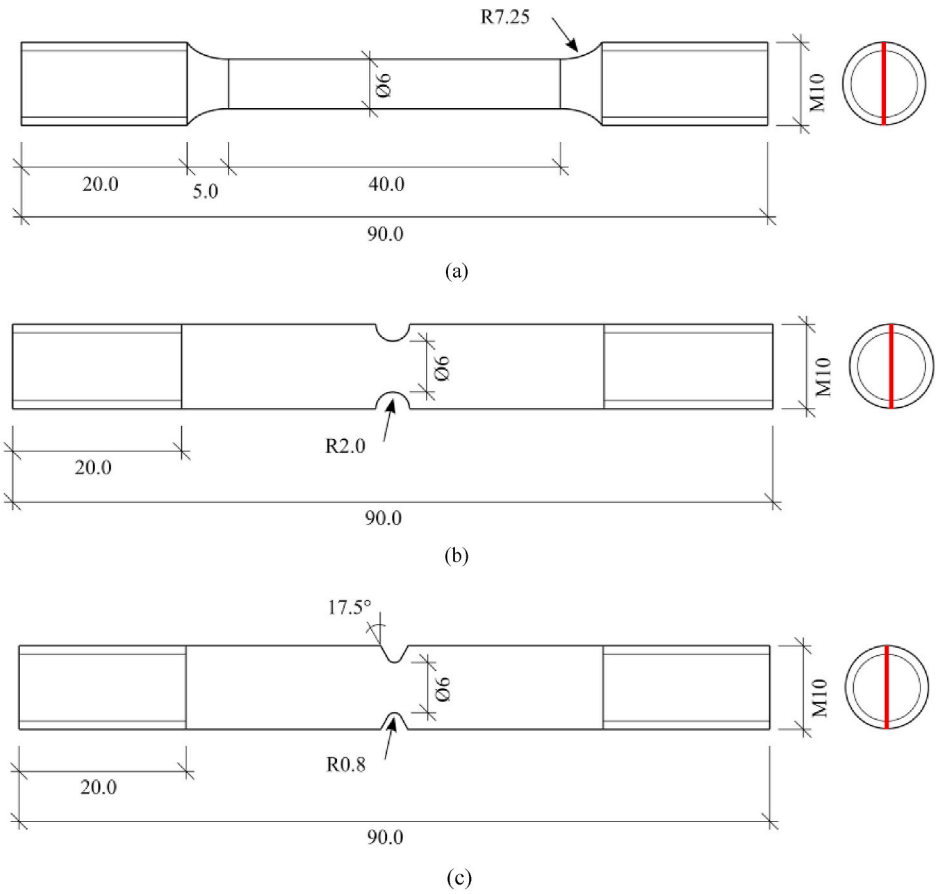

Fig. 1. Nominal geometry of the test specimens used for the cast and homogenised alloys: a) smooth specimen, b) notched specimen R2.0 with notch radius of 2.0 mm, and c) notched specimen R0.8 with notch radius of 0.8 mm. The red line denotes the radial direction of the DC-cast billet and was marked physically on the specimen. All measures are in mm. (For interpretation of the references to colour in this figure legend, the reader is referred to the Web version of this article.)

3. Results

3.1. Microstructure

3.1.1. Cast and homogenised condition

Fig. 3 presents images of the grain structure of the four cast and homogenised alloys. The grain structure of all four alloys is dendritic, which is typical for cast and homogenised aluminium alloys. Visual inspection indicates that the grain size is similar for the A- and B-variants. Although particles are visible in all four images, the two B-variants have a substantially larger number of visible particles than the respective A-variants. No measurements were performed to determine the crystallographic texture of the cast and homogenised alloys. However, a random texture can be assumed for alloys in the cast and homogenised condition and thus their behaviour is considered to be isotropic [33].

The average grain size D_g (assuming equi-axed grains), the area fraction of constituent particles f_p, and the average particle size D_p (defined as the area average of the equivalent particle diameter D_{eq}) are presented in Table 2. A minor difference in grain size is observed between the A- and B-variants of both alloy 6063 and alloy 6110. The area fraction of constituent particles of the B-variant is on average 3.1 times larger than for the A-variant of the same alloy. While the average particle size D_p decreases from alloy 6110A to alloy 6110B, it remains the same for the alloys 6063A and 6063B. In addition to the aforementioned metrics, the area averaged maximum and minimum Feret diameters of the constituent particles, denoted $D_{f,max}$ and $D_{f,min}$, respectively, were calculated from the SEM images. These two metrics of the constituent particles are similar for the A- and B-variants of alloy 6063 as well as for alloy 6110, with differences less than 5%. Measurements of all four cast and homogenised alloys show that the constituent particles have random orientation.

Fig. 4 displays the PSDs of constituent particles for the cast and homogenised alloys. The particle population of alloy 6063B is slightly shifted towards larger particles compared with alloy 6063A, while a marked shift towards smaller particles is observed for alloy 6110B compared with alloy 6110A. It should be noted that the number of particles in every size group is much higher for the B-variant than for the A-variant of both alloys, as the area fraction of particles is on average 3.1 times larger for the former.

Fig. 5a and Fig. 5b display the PCFs for the alloys 6063A and 6063B, respectively. Both PCFs display a tendency of circular clustering around the centre. This circular pattern may be attributed to the random structure of the grains, as constituent particles form mainly at the dendrite and grain boundaries during solidification [27]. The difference in smoothness between the two PCFs is presumably due to the larger sample size used to obtain Fig. 5b, as well as the generally higher level of particle clustering in the B-versions of the alloys.

The PCFs of the cast and homogenised 6110A and 6110B alloys are shown in Fig. 6a and Fig. 6b, respectively. The intensity of the PCFs for the 6110 alloys in Fig. 6 is clearly stronger around the centre than the PCFs for the 6063 alloys in Fig. 5. The strong intensity for the B alloys is linked to the clustering of smaller particles ($D_{eq}<1$ μm), which is readily seen if these smaller particles are omitted from the computation of the PCFs. It was found that the clustering of larger particles ($D_{eq}>1$ μm) is markedly stronger for alloy 6063B than for alloy 6110B. Also, the area fraction of particles of the two B-alloys is identical provided smaller particles are disregarded, with values of 0.0156 and 0.0155 for the alloys 6063B and 6110B, respectively.

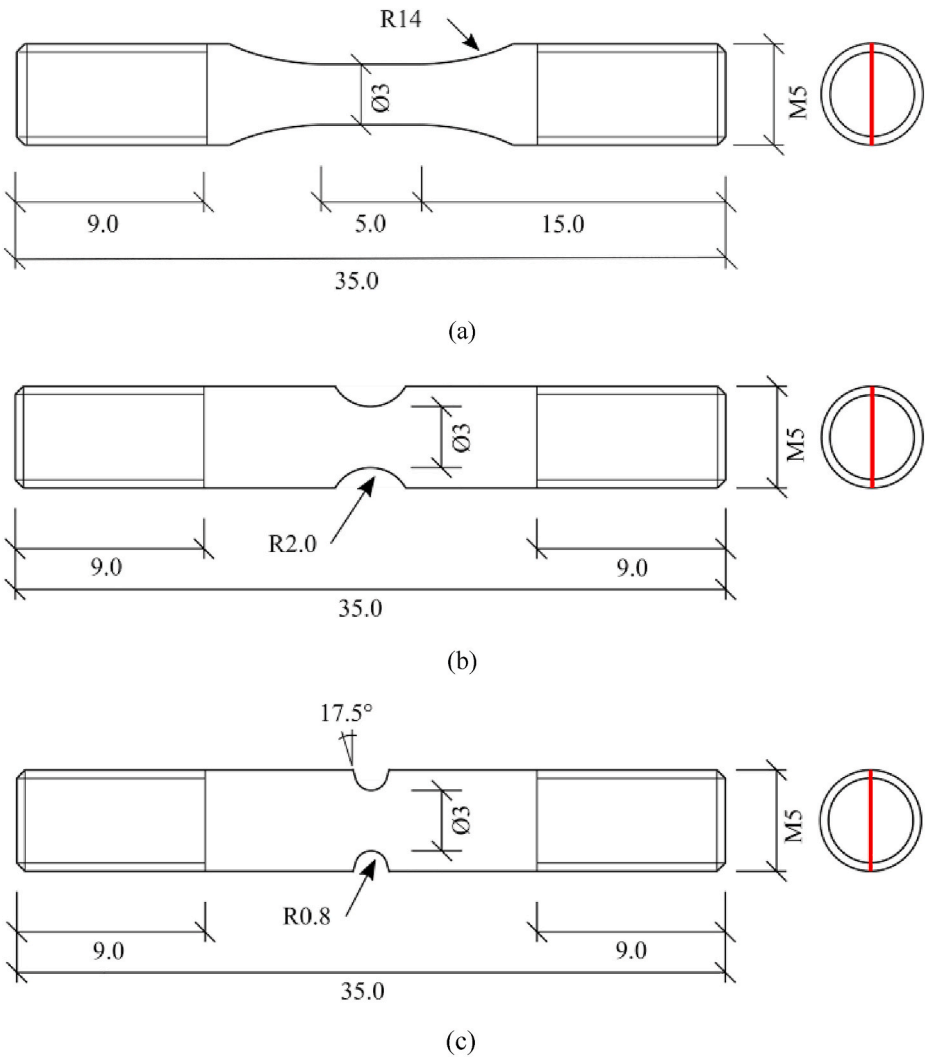

Fig. 2. Nominal geometry of the test specimens used for the extruded alloys: a) smooth specimen, b) notched specimen R2.0 with notch radius of 2.0 mm, and c) notched specimen R0.8 with notch radius of 0.8 mm. The red line denotes the ND of the extruded profiles and was marked physically on the specimens. All measures are in mm. (For interpretation of the references to colour in this figure legend, the reader is referred to the Web version of this article.)

SEM images of the constituent particles in the cast and homogenised 6110 alloys are presented in Fig. 7. As expected from the PCFs, the constituent particles do not have any preferential orientation, but they form in randomly oriented elongated clusters. Both smaller and larger constituent particles are visible for both the A- and B-variants of the 6110 alloy. The marked shift in the PSD of alloy 6110B, see Fig. 4b, is attributed to the highly numerous and clustered smaller particles visible in Fig. 7b. Similar SEM images were obtained for the 6063 alloy, but are not shown here for brevity. Dispersoids are visible in the SEM images of the 6110 alloys, and these are evenly distributed throughout the matrix material.

3.1.2. Extruded condition

Fig. 8 shows images of the grain structure of the four extruded alloys. It is apparent that there are two different grain structures caused by the extrusion process. The 6063 alloys display a recrystallised grain structure, while the 6110 alloys display a non-recrystallised, fibrous grain structure with grains that are severely elongated in the ED.

The ODFs for the B-variants of the extruded alloys are shown in Fig. 9. These ODFs are representative also for the A-variants because the difference in crystallographic texture between the A- and B-variants was minor for both the 6063 and 6110 alloys. The 6063 alloys exhibit a typical recrystallisation texture, i.e., a strong cube texture with a minor Goss component. In contrast, the 6110 alloys display a cube texture with orientations along the β-fibre, which is typically found in non-recrystallised extruded aluminium alloys.

The average grain dimensions in the ND and TD of the extruded alloys are presented in Table 3 along with the area fraction of particles f_p, the average particle size D_p, and the maximum and minimum Feret diameters $D_{f,max}$ and $D_{f,min}$ of the particles in the ED-ND and TD-ND planes. For both alloys, the grain size is reduced after extrusion, but particularly for the non-recrystallised 6110 alloys. The extrusion process breaks up the particles of the cast and homogenised alloys and as a result, the particle size is substantially reduced in the extruded condition. The average particle size D_p is somewhat larger for the B-variants than for the A-variants of both extruded alloys. Whereas the area fraction of particles f_p of the A-variants is about the same for the cast and homogenised condition and the extruded condition, it is somewhat higher for the extruded B-variants than for the cast and homogenised counterparts, see Tables 2 and 3. This difference in f_p is attributed to the sample size and the accuracy of the characterisation technique. The maximum Feret diameter is somewhat larger in the ED-ND plane than in the TD-ND plane, while the minimum Feret diameter is about the same in the two planes.

The PSDs shown in Fig. 10 for the extruded alloys reflect the change in the average particle size D_p due to the extrusion process, and are thus

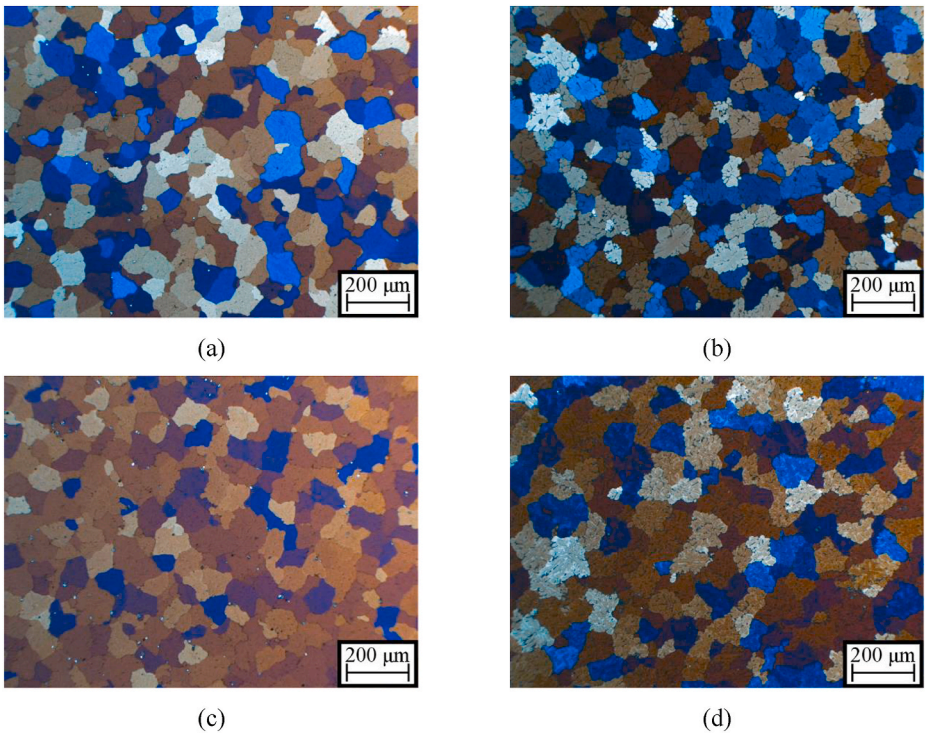

Fig. 3. Grain structure of the four cast and homogenised alloys: (a) 6063A, (b) 6063B, (c) 6110A, and (d) 6110B.

Table 2
Selected microstructural quantities of the alloys in the cast and homogenised condition.

Alloy	D_g [μm]	f_p [−]	D_p [μm]	$D_{f,max}$ [μm]	$D_{f,min}$ [μm]
6063A	63	0.0061	1.64	3.37	1.17
6063B	58	0.0198	1.67	3.45	1.31
6110A	67	0.0076	1.85	3.70	1.42
6110B	72	0.0226	1.53	3.53	1.47

shifted towards smaller particle sizes compared to the PSDs of the corresponding alloys in the cast and homogenised condition, see Fig. 4. The PSDs of the A- and B-variants of an alloy are similar, with only a minor shift towards larger particles for the latter.

Fig. 11 shows the PCFs for the B-variant of the extruded 6110 alloy in the TD-ND and ED-ND planes, which are characteristic for all the extruded alloys. The PCF in the TD-ND plane shows a weak clustering along the TD, in the vicinity of the centre, while in the ED-ND plane there is a prominent clustering along the ED. The latter is an indication of particles aligned in stringers along the ED. By comparing Figs. 6 and 11, it appears that the extrusion process has redistributed the particles as expected.

SEM images of the constituent particles in the TD-ND and ED-ND planes of the extruded 6110B alloy are presented in Fig. 12. The constituent particles are more homogeneously dispersed throughout the matrix than in the corresponding cast and homogenised alloy, see Fig. 7b. This change was also indicated by the PCFs in Fig. 11 due to the overall lower intensity in the figure. Both the SEM image and the PCF of the ED-ND plane show that the constituent particles tend to cluster along the ED, albeit the tendency is weaker than the clustering observed in the cast and homogenised condition. Similar images were obtained for the other extruded alloys, but these are omitted due to brevity as the overall trends are the same. Dispersoids were observed in the SEM images of both 6110 alloys, as fine particles which are evenly dispersed in the matrix material.

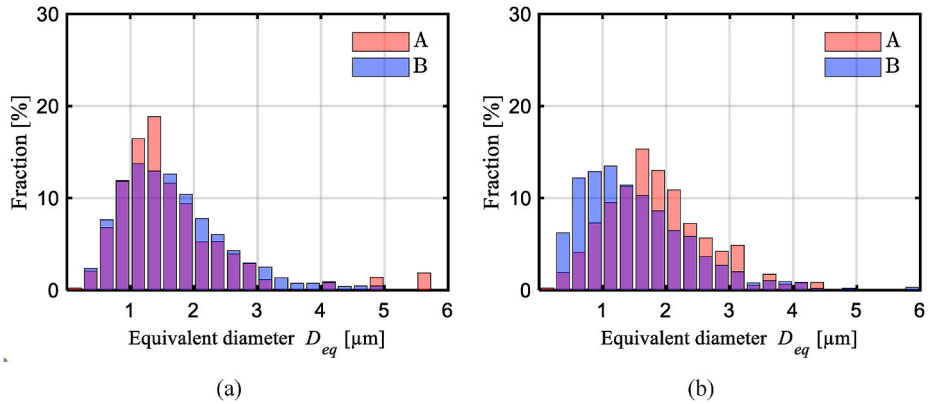

Fig. 4. Particle size distributions (PSDs) for the A- and B-variants of the cast and homogenised alloys: (a) 6063, and (b) 6110.

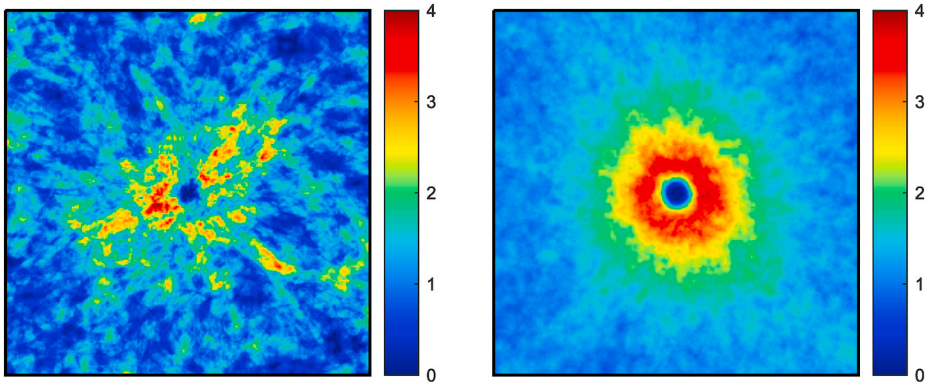

Fig. 5. Pair correlation functions (PCFs) for the cast and homogenised alloys computed from a 20 μm × 20 μm square: (a) 6063A, and (b) 6063B.

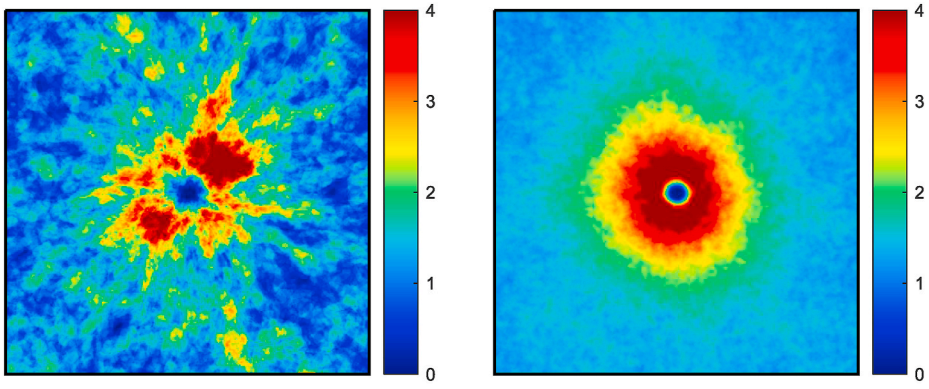

Fig. 6. Pair correlation functions (PCFs) for the cast and homogenised alloys computed from a 20 μm × 20 μm square: (a) 6110A, and (b) 6110B.

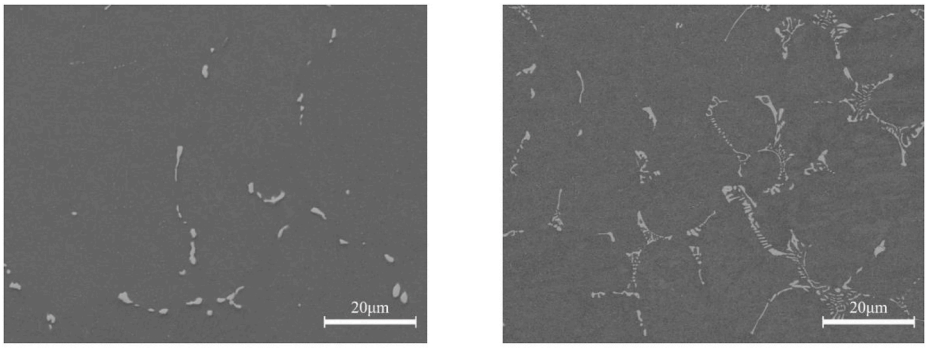

Fig. 7. SEM images showing the constituent particles of the cast and homogenised alloys: (a) 6110A, and (b) 6110B.

3.2. Mechanical test results

In the following, the stress-strain curves, defined in terms of the true stress and the logarithmic strain, are presented for the A- and B-variants of the cast and homogenised alloys and the extruded alloys. The stress-strain curves of the A- and B-variants are given by red and blue solid lines, respectively. The specimen geometry is identified by the marker at the point of failure, i.e., at the maximum value of the true stress where strain softening starts. The markers × , ◊ and ○ correspond in turn to results obtained with smooth specimens and notched specimens with notch radius 2.0 mm (R2.0) and 0.8 mm (R0.8), respectively. In addition to the stress-strain curves, a selection of SEM images of fracture surfaces that show distinctive features is presented.

To illustrate the typical behaviour observed for the various alloys after failure, i.e., in the softening branch of the response curve, some representative stress-strain curves are presented in Fig. 13. All four response curves are plotted to fracture, which is defined as separation of the specimen into two halves, whereas the markers denote the point of failure. The cast and homogenised alloys fracture shortly after the point of failure, while the extruded alloys typically fracture after significant additional straining. The amount of straining after failure is seen to depend on both specimen geometry, alloy and processing. In the

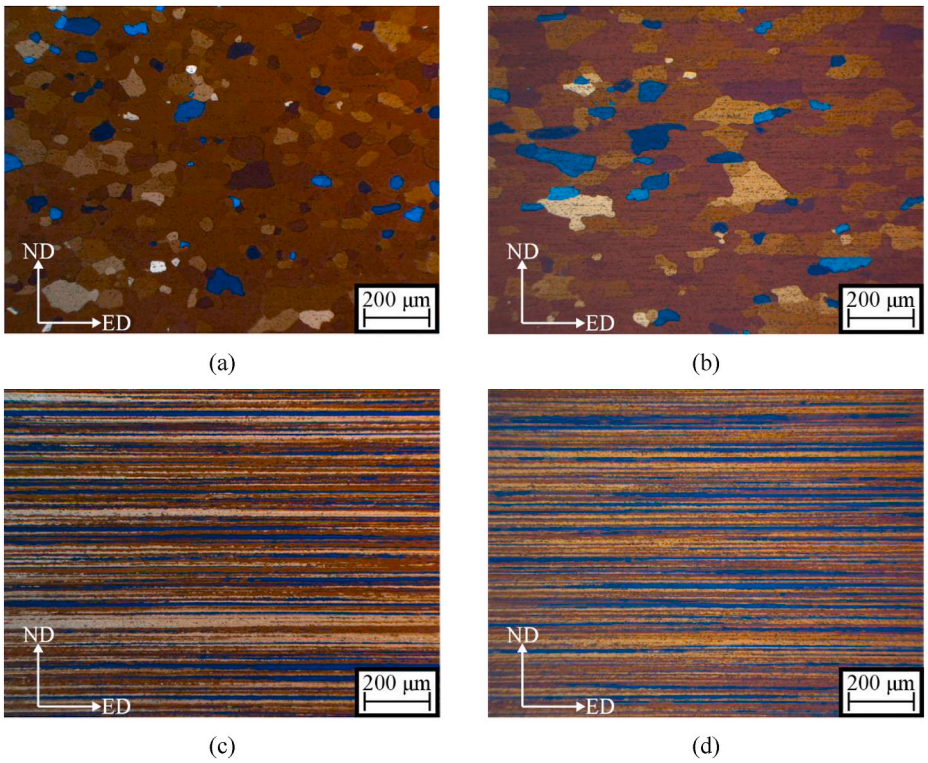

Fig. 8. Grain structure of the extruded alloys: (a) 6063A, (b) 6063B, (c) 6110A, and (d) 6110B.

following, the stress-strain curves are plotted to failure, as this denotes the critical point from a structural engineering perspective.

3.2.1. *Cast and homogenised condition*

Fig. 14 displays the stress-strain curves of the cast and homogenised 6063 alloys. The 0.2% proof stress, $\sigma_{0.2}$, is around 12.5 MPa higher for alloy 6063B than for alloy 6063A, and a somewhat higher initial hardening rate is seen in uniaxial tension for the former. The flow stress is markedly higher for the notched specimens due to the triaxial stress field induced by the pre-machined notch and is highest for the R0.8 specimen which has the smallest notch radius. For both the A- and B-variants of the alloy, the failure strain is significantly higher for the smooth specimen than for the two notched specimens, but somewhat unexpectedly, the R0.8 specimen has a higher failure strain than the R2.0 specimen. The notch effect on ductility, hereby denoted notch sensitivity and defined as the percentage reduction in failure strain of the notched specimens relative to the smooth specimen, is significant for both alloy 6063A and alloy 6063B. The two alloys follow similar trends where the notch sensitivity is somewhat stronger for the R2.0 specimen than for the R0.8 specimen. For all specimen geometries, the A-variant of the alloy has the highest ductility. Comparing the smooth specimens, the B-variant of the 6063 alloy has an average failure strain that is 72.3% of the average failure strain of the A-variant. For the notched specimens, the difference in ductility between the A- and B-variants is even larger, and largest for the R0.8 specimen.

The stress-strain curves of the cast and homogenised 6110 alloys are shown in Fig. 15, and similar trends as for the 6063 alloys are found. There is a difference in the proof stress of 12 MPa between the A- and B-variants of the alloy, which is accompanied by a notable difference in hardening rate. The B-variant exhibits a higher hardening rate for small strains, while at larger strains the hardening rate is higher for the A-variant. Remarkably, the failure strain observed for the smooth specimens of the B-variant of alloy 6110 is only half of the failure strain of the A-variant. Similar differences in tensile ductility are observed also for the two notched specimens. The notch sensitivity is significant and the A- and B variants follow similar trends, just as for the 6063 alloys. However, for the 6110 alloys the notch sensitivity of the two notched specimens is more similar.

One specimen from each combination of alloy and geometry was assessed using an SEM. All fracture surfaces displayed a typical dimpled surface associated with ductile fracture. The outer circumference of the fracture surfaces was circular, indicating isotropic behaviour. Fig. 16 displays two SEM images, which are representative of the fracture surface topology. The fracture surfaces in the figure exhibit two populations of dimples. The first is the evenly dispersed large- and normal-sized dimples, and the second is the high density of small-sized shallow dimples. It is worth noting that particles are visible at the bottom of the dimples.

3.2.2. *Extruded condition*

Fig. 17 shows the stress-strain curves in the 0° and 90° directions of the extruded 6063 alloys. The difference in the 0.2% proof stress between the A- and B-variants is 10.2 MPa and 11.8 MPa for the 0° direction and the 90° direction, respectively. The yield stress is highest in the ED, and there is a difference in the proof stress of 12.7 MPa between the two directions for the A-variant. The initial hardening rate is similar for the two variants in both directions, while at a later stage the A-variant has a slightly lower hardening rate than the B-variant.

As for the cast and homogenised alloys, the B-variant of the 6063 alloy has lower ductility than the A-variant in uniaxial tension, but the difference is much smaller. The average failure strain of the B-variant is 12.8% lower in the 0° direction and 16.8% lower in the 90° direction compared to the A-variant. There is also a difference in ductility between the tests in the two directions, and the failure strain in uniaxial tension is 10.6% and 5.6% higher in the 90° direction for the A- and B-variants, respectively. The notch sensitivity is very strong in both tensile directions, and in all cases the failure strain is reduced by more than 70% due to the pre-machined notch. It is further interesting to note that the notch sensitivity is consistently larger for the A-variant than for the B-variant of the 6063 alloy. Indeed, for both notch geometries in the

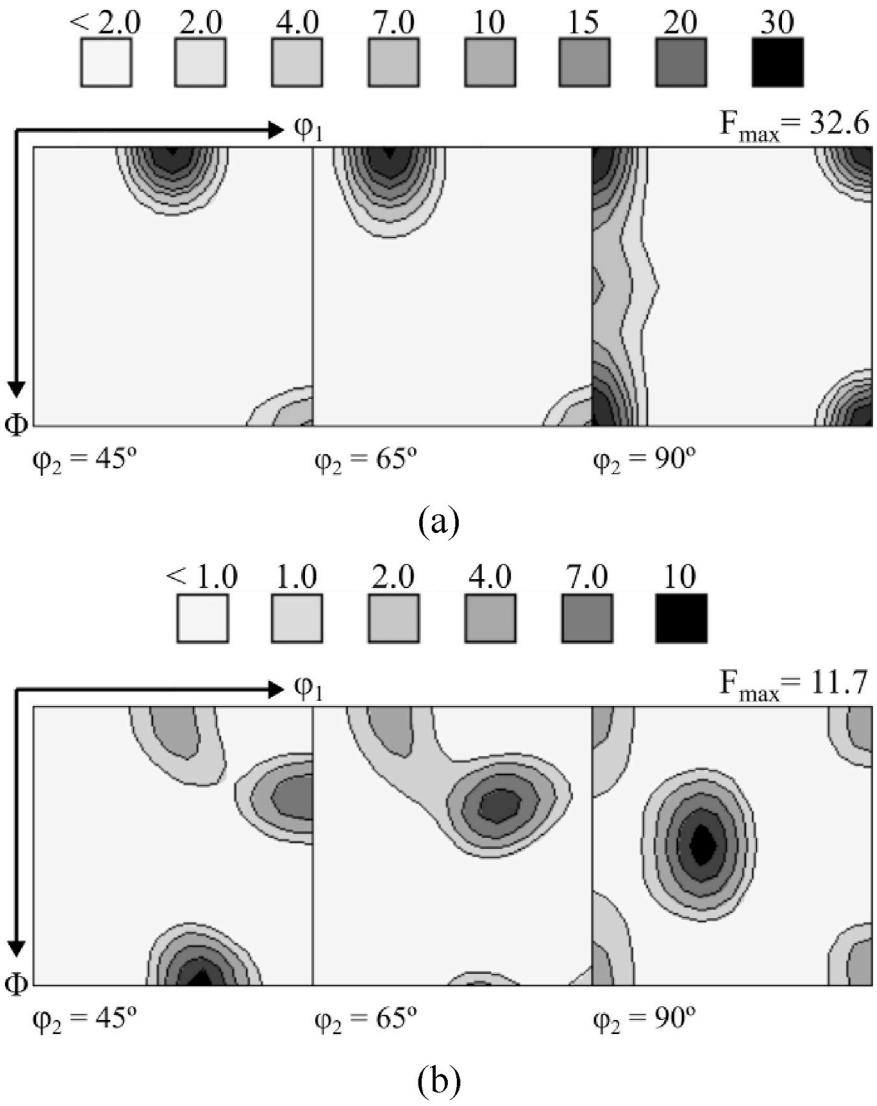

Fig. 9. Orientation distribution functions (ODFs) for the B-variants of the extruded alloys: (a) 6063B, and (b) 6110B.

Table 3
Selected microstructural quantities of the alloys in the extruded condition.

Alloy	D_g [μm]		f_p [−]	D_p [μm]	$D_{f,max}$ [μm]		$D_{f,min}$ [μm]	
	ND	TD			TD-ND	ED-ND	TD-ND	ED-ND
6063A	30	36	0.0063	1.05	1.89	2.61	0.74	0.84
6063B	30	41	0.0242	1.17	1.89	2.58	0.92	0.98
6110A	4	8	0.0079	1.13	1.74	2.49	0.91	1.01
6110B	3	6	0.0301	1.22	2.05	2.32	1.02	0.99

0° direction and for the R0.8 specimen in the 90° direction, the failure strain is larger for the B-variant than for the A-variant of the alloy, which was clearly unexpected. While the two notch geometries give similar ductility in the 0° direction, the R0.8 specimen gives markedly lower ductility in the 90° direction relative to the R2.0 specimen. Compared with the 0° direction, the ductility in the 90° direction is higher for the R2.0 specimen and lower for the R0.8 specimen.

Fig. 18 presents the results of the test series of the extruded 6110 alloys. For both the 0° and 90° directions, there are no significant differences in neither the 0.2% proof stress nor the hardening rate between the A- and B-variants of the alloy. The 0.2% proof stress is 17 MPa higher in the 0° direction than in the 90° direction for the A-variant, and 13 MPa higher for the B-variant. Alloy 6110B has markedly lower failure strain in uniaxial tension for both the 0° and 90° directions when compared to alloy 6110A, and the difference is 17% in both directions. The difference in the failure strain in uniaxial tension between the two directions is minor and deemed statistically insignificant. A marked notch sensitivity is observed also for the 6110 alloys. The ductility relative to the smooth specimen is reduced with more than 50% in the 0° and 90° directions for both the A- and B-variants, and the notch sensitivity is somewhat stronger in the 90° direction. For the 6110 alloy, the failure strain is found to consistently decrease with decreasing notch radius for both geometries and tensile directions. It is also notable that the notch sensitivity is markedly stronger for the recrystallised 6063 alloys than for the non-recrystallised 6110 alloys. Indeed, for the notched specimens the ductility is generally higher for the 6110 alloys than for the 6063 alloys, while for the smooth specimens the ductility is substantially higher for the leaner 6063 alloys.

In general, the fracture surfaces display a circular or elliptical outer circumference. However, the fracture surfaces of the notched specimens of the extruded 6063A alloy machined in the 90° direction developed a more rhombus shape. As a result, the logarithmic strain calculated for these specimens is uncertain after the rhombus shape starts to form at large strains. Frodal et al. [7] found that the strain calculated based on the assumption of an elliptical outer circumference underestimated the

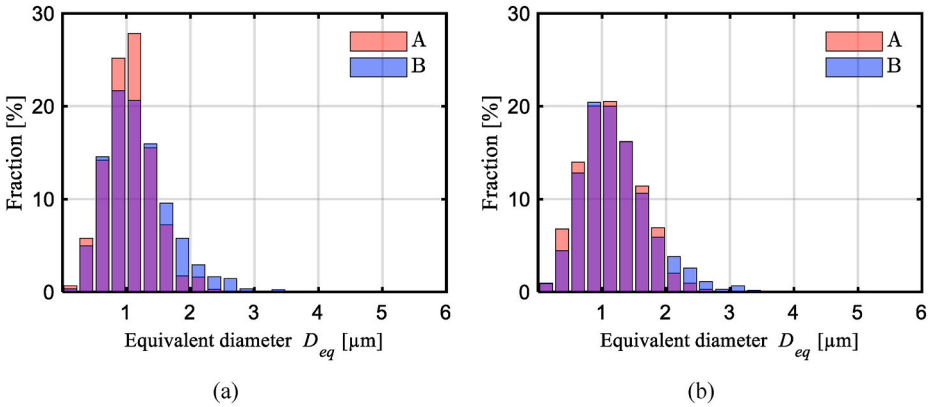

Fig. 10. Particle size distributions for the A- and B-variants of the extruded alloys: (a) 6063, and (b) 6110.

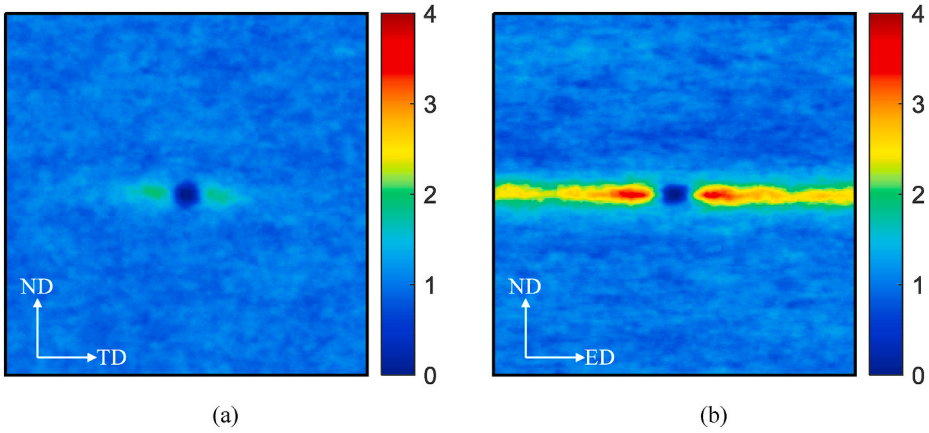

Fig. 11. Pair correlation functions (PCFs) for the extruded 6110B alloy computed from a 20 μm × 20 μm square: (a) TD-ND plane, and (b) ED-ND plane.

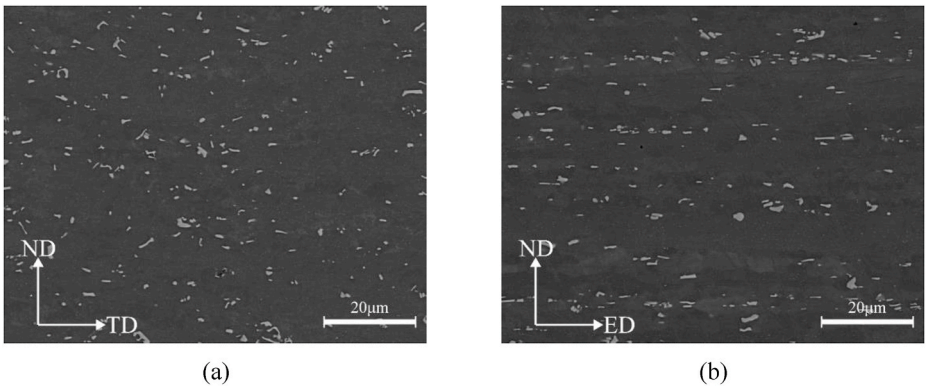

Fig. 12. SEM images showing the constituent particles in (a) the TD-ND plane and (b) the ED-ND plane of the extruded 6110B alloy.

real strain by less than 10%.

Fig. 19 shows four distinctive features found in the fracture surfaces of the extruded alloys based on SEM investigations. The figure includes what has previously been characterised as an oversized dimple (Fig. 19a), intergranular fracture in the form of facets (Fig. 19b), an almost continuous line of particle-filled dimples also known as a stringer (Fig. 19c) and, lastly, the two characteristic dimple populations observed (Fig. 19d).

Both oversized dimples and facets are prominent features in the 6063 alloys, but not in the 6110 alloys. Oversized dimples were mainly observed on the fracture surface of the smooth specimens, and Westermann et al. [27] attribute these to voids nucleated at grain boundaries which grow into the two neighbouring grains. In contrast, facets are mainly seen for the notched specimens, and appear to be more frequent for the 0° specimens than for the 90° specimens. They also occur more frequently on the fracture surfaces of alloy 6063A relative to alloy 6063B. Facets have previously been linked to excess Si forming brittle particles at the grain boundaries by Kato et al. [22], Remøe et al. [23] and Aucote and Evans [34], which agrees well with the high Si/Mg ratio of the 6063 alloys [28]. Facet-like structures are seen at the bottom of some of the oversized dimples, which could indicate that the facets and the oversized dimples have the same source. The fracture surface of the smooth specimens of alloy 6063A in the 0° direction appears to have the highest population of oversized dimples, while the population is

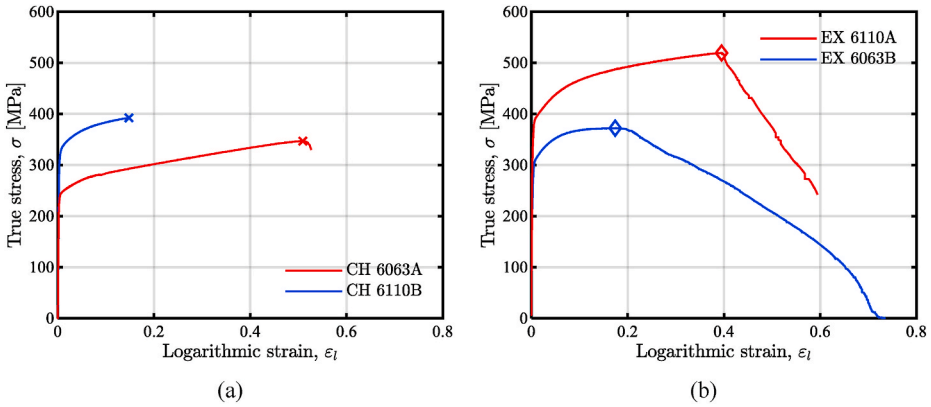

Fig. 13. Representative true stress versus logarithmic strain curves displaying typical behaviour after failure, which is denoted by the markers: (a) cast and homogenised smooth specimens, and (b) extruded R2.0 specimens in the 0° direction.

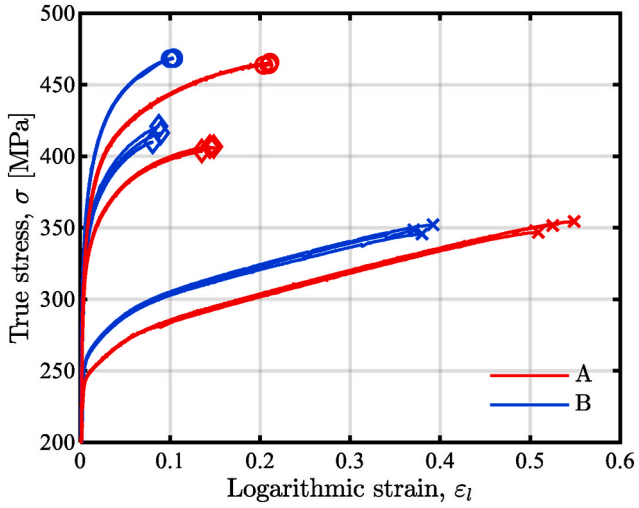

Fig. 14. Stress-strain curves of the cast and homogenised 6063 alloys, where the failure strain is indicated by a marker that changes depending on the specimen geometry: × - Smooth, ◊ - R2.0, ○ - R0.8.

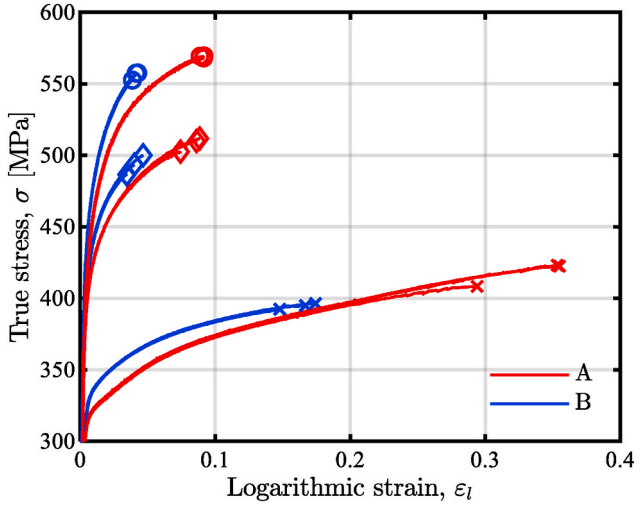

Fig. 15. Stress-strain curves of the cast and homogenised 6110 alloys, where the failure strain is indicated by a marker that changes depending on the specimen geometry: × - Smooth, ◊ - R2.0, ○ - R0.8.

somewhat lower for alloy 6063A in the 90° direction and about the same for alloy 6063B in both directions.

While stringers aligned in the ED are present on the fracture surfaces of the 90° specimens for all alloys, the one shown in Fig. 19c is the most pronounced stringer observed in all test series. The almost continuous line of particles is measured to be over 200 μm long and is filled with densely packed constituent particles. Both the PCF in Fig. 11b and the SEM image in Fig. 12b indicate that constituent particles of the extruded alloys have a tendency to cluster along the ED, which suggests that stringers originate from these clusters.

Fig. 19d shows the two populations of dimples present in all the extruded alloys, and it displays one of the cases with the highest amount of the smaller dimples. However, such zones with large amount of small and numerous dimples appear to be much more prevalent in the 6110 alloys than in the 6063 alloys. A possible explanation for this observation is the high density of dispersoids in the 6110 alloys, which could play a role at a late stage of the fracture process [35,36].

4. Discussion

To study the influence of the volume fraction of constituent particles on the ductility, two engineering alloys and two tailor-made alloys with higher amounts of Fe and Si were considered. While the strength and work hardening differed somewhat between the engineering and tailor-made alloys (i.e., the A- and B-variants), cf. Figs. 14 and 15 for the cast and homogenised alloys and Figs. 17 and 18 for the extruded alloys, the differences were deemed sufficiently small to not play a major role for the ductility and the fracture mechanisms. Thus, the differences seen in ductility and fracture mechanisms between the engineering and tailor-made alloys are assumed to be largely determined by the volume fraction, size distribution and spatial distribution of the constituent particles, whereas differences in strength and work hardening play a minor role.

The uniaxial tension tests presented in Figs. 14 and 15 display a clear reduction in failure strain of the cast and homogenised alloys with increased amount of constituent particles. The influence of the area fraction of particles is strongest for the 6110 alloy, which is assumed caused by the higher strength, although other variables cannot be dismissed such as the more clustered population of smaller particles of the 6110B alloy, and possible differences in chemical composition of the constituent particles.

The influence of the machining error (see Section 2.3) upon the stresses and strains for the notched specimens, which were machined from the two cast and homogenised A-alloys, was examined by Thomesen [37]. It was found by numerical simulations that the stress level of the R0.8 specimens may experience a reduction of 15–20 MPa due to the deviation in outer diameter, while the stress level of the R2.0

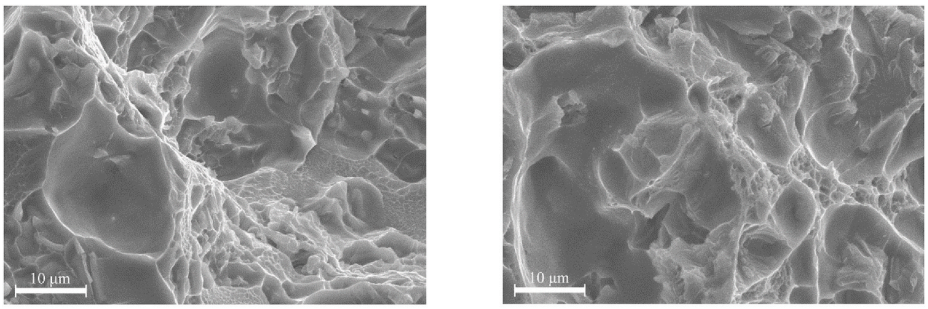

Fig. 16. Representative images of the fracture surfaces for the cast and homogenised alloys: (a) alloy 6063B, R2.0 specimen, and (b) alloy 6110B, R0.8 specimen.

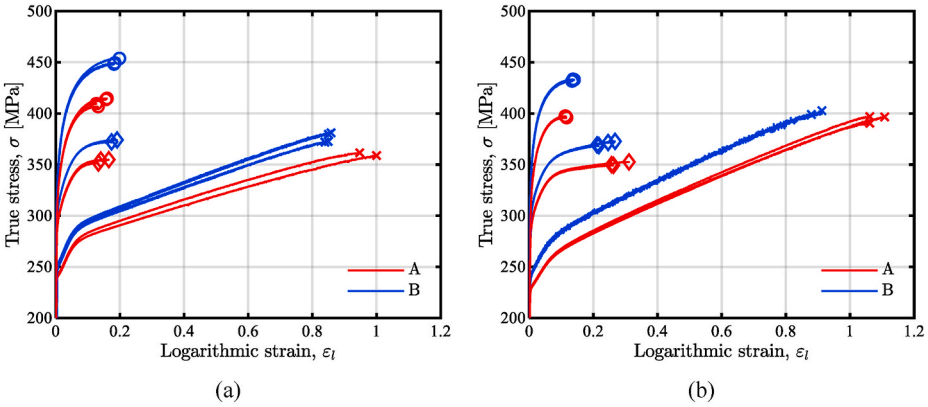

Fig. 17. Stress-strain curves in the (a) 0° and (b) 90° directions for the extruded 6063 alloys, where the failure strain is indicated by a marker that changes depending on the specimen geometry: × - Smooth, ◊ - R2.0, ○ - R0.8.

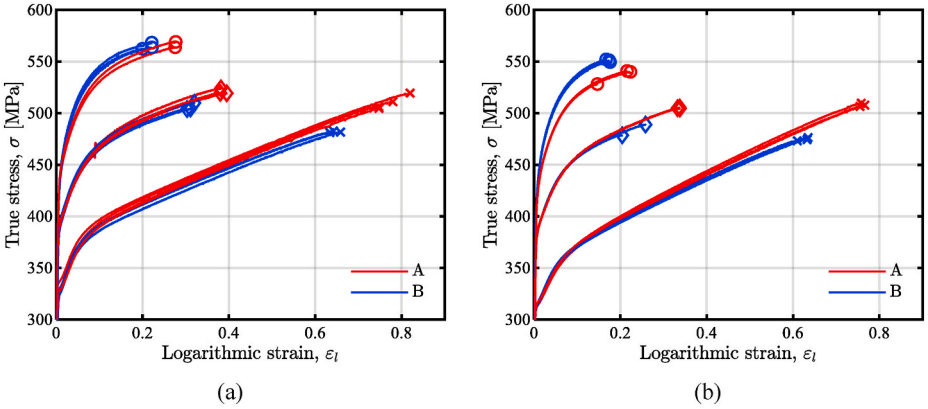

Fig. 18. Stress-strain curves in the (a) 0° and (b) 90° directions for the extruded 6110 alloys, where the failure strain is indicated by a marker that changes depending on the specimen geometry: × - Smooth, ◊ - R2.0, ○ - R0.8.

specimens was not affected. Thomesen [37] also conducted an experimental assessment of the deviation in outer geometry using specimens machined from a cast and homogenised AA6061 alloy, and found that the failure strain was sensitive to the changes in the outer diameter. The maximum observed difference in failure strain was notable, but much less than the deviation between the A- and B-alloys observed in Figs. 14 and 15. Thus, the large difference in the failure strain of the notched specimens made of the cast and homogenised A- and B-alloys is mainly attributed to the different volume fraction of constituent particles, whereas the slight difference in specimen geometry plays a secondary role.

When considering the uniaxial tension tests of the extruded alloys presented in Figs. 17 and 18, there is a substantial overall increase in failure strain for all alloys relative to their cast and homogenised counterpart. While the geometry of the smooth tensile specimens was different in the two test series, it was found by Thomesen et al. [31] to have no influence on the measured failure strain. The increase is by far the largest for the 6110B alloy, where the failure strain is almost four times higher in the extruded condition. For the other three alloys, the failure strain is about twice as high after extrusion. The non-recrystallised grain structure of the two 6110 alloys after extrusion is likely an important contributor to the overall larger increase in failure strain of the extruded 6110 alloys. Further, it is apparent that the higher volume fraction of constituent particles in the B-variants of the extruded

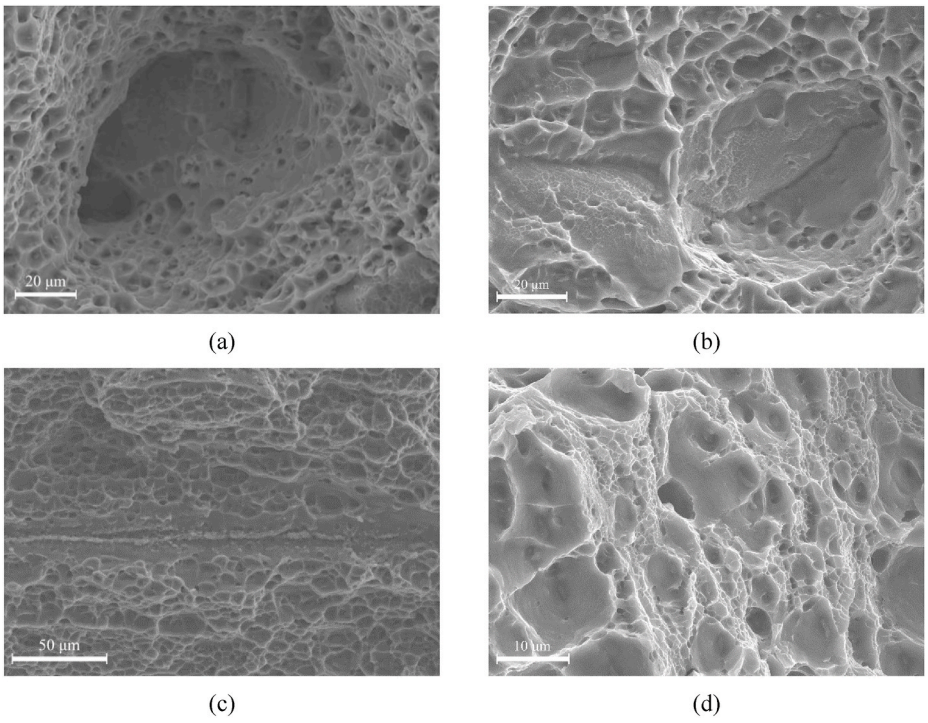

Fig. 19. Representative images of the fracture surfaces of the extruded alloys: (a) alloy 6063B, smooth specimen, 90° direction, (b) alloy 6063B, R0.8 specimen, 90° direction, (c) alloy 6110B, R2.0 specimen, 90° direction, and (d) alloy 6110A, R2.0 specimen, 0° direction.

alloys decreases the failure strain when compared to the corresponding A-variant, but the difference is considerably less in the extruded condition than in the cast and homogenised condition. From Tables 2 and 3 it is apparent that the extrusion processes reduces the constituent particle size, and the redistribution of the constituent particles due to the extrusion process is clearly seen from the PCFs presented in Figs. 6 and 11. As a result of the redistribution, the alloys experience significantly less prominent clustering as the particles are more homogeneously distributed in the volume. As the area fraction of constituent particles does not change with extrusion, the overall reduction in size and the more favourable spatial distribution of the constituent particles are assumed to cause the observed smaller difference in failure strain between the A- and B-alloys after extrusion.

All four alloys, in both conditions, show a pronounced reduction in the failure strain in the notch tension tests compared to uniaxial tension tests. The increased stress triaxiality caused by the notch has a clear detrimental effect upon the ductility. For the cast and homogenised alloys, as well as for the extruded 6110 alloys, the notch sensitivity of the B-variant is higher than that of the A-variant, while for the extruded 6063 alloys the opposite is true. This finding is presumably linked to the facets observed on the fracture surface of the extruded 6063 alloys. Prior to extrusion the 6110 alloys displayed a higher notch sensitivity than the 6063 alloys, while after extrusion the notch sensitivity of 6110 was greatly improved. The improvement of the notch sensitivity of the 6110 alloys is likely caused by the non-recrystallised grain structure. Overall, the difference in notch sensitivity between the corresponding A- and B-alloys is rather small, indicating that the constituent particle content does not influence the notch sensitivity.

For the extruded 6110 alloys, the failure strain in uniaxial tension is similar in the two directions investigated, whereas in the notch tension tests the failure strain is higher in the 0° direction. Some of the factors that could contribute to the lower ductility in the 90° direction are the shape of the particles, being longer in the ED than in the TD, and the particle stringers aligned with the ED (see Fig. 19c). Lassance et al. [10] observed that the orientation of the constituent particles influences the nucleation of voids, and Benzerga et al. [16] found that the void growth is inherently anisotropic due to anisotropic plastic flow. Intra- and inter-cluster coalescence may also cause failure anisotropy due to the direction of the tensile load relative to the orientation of the cluster(s), see e.g. Hannard et al. [20] and the numerical work of Thomson et al. [38] and Steglich et al. [39]. More recently, in-situ experiments conducted by Kondori et al. [21] show that the mechanisms of coalescence are anisotropic. Dilatational void growth is enhanced by increasing triaxiality, while extensional void growth is dominant at lower levels of stress triaxiality [15,16] and void nucleation is dependent upon stress level [6,10,11]. It seems reasonable to assume that the mechanisms leading to anisotropic void nucleation and coalescence are more dominant for higher stress triaxiality, and thereby explaining why the ductility is higher in the 0° direction for the notched specimens but not for the smooth specimens.

The failure strain is generally slightly higher in the 90° direction than in the 0° direction for the extruded 6063 alloys; an exception is the R0.8 specimen for which the failure strain is somewhat higher in the 0° direction. It is likely that the mechanisms discussed for the extruded 6110 alloys are also valid for the extruded 6063 alloys. The higher work hardening rate in the 90° direction is a factor that could contribute to a higher ductility as it is known to distribute the plastic flow more evenly and thus delay plastic instability and strain localisation [40]. Fig. 17 shows that the failure strain in the notch tension tests is, with one exception, somewhat larger for the extruded 6063B alloy than for the 6063A alloy, even if the particle content is more than three times larger in the former and the strength is also slightly higher. The reason for this anomaly is believed to be linked to the facets on the fracture surfaces which where markedly more frequent for the notch tension tests of the 6063A alloy, indicating a higher percentage of intergranular fracture.

Several notch tension tests of the R0.8 specimen display an equal or higher failure strain than the tests of the R2.0 specimen for the same alloy, as seen in Figs. 14 and 15 for the cast and homogenised alloys and in Fig. 17 for the extruded 6063A alloy. It is anticipated that a sharper notch will increase the overall stress triaxiality in the notch region and thus the R0.8 specimen was expected to give a lower failure strain than the R2.0 specimen. Numerical simulations performed by Thomesen [37]

show that the stress triaxiality is highest in the centre of the notched specimens (see also Børvik et al. [41]). The equivalent plastic strain remains fairly even from the centre towards the notch root of the R2.0 specimen, while it is highest at the notch root for the R0.8 specimen. As ductile damage growth is governed by plastic straining, but amplified by the stress triaxiality [42], the location of fracture initiation may shift from the centre for the R2.0 specimens towards the notch root for the R0.8 specimen. Kondori et al. [21] also observed that fracture initiated close to the notch root for specimens with a sharp notch. This possible change of failure mode may explain why the failure strain is equal or even larger for the R0.8 specimen than for the R2.0 specimen in several cases.

5. Conclusion

The effects of constituent particle content on ductile fracture in typical 6000-series aluminium alloys were studied by performing tension tests on smooth and notched specimens on two engineering alloys (i.e., 6063A and 6110A) and two similar tailor-made alloys (i.e., 6063B and 6110B) with more than three times higher area fraction of particles. Tests were conducted for the alloys in the cast and homogenised condition and the extruded condition, in both cases after artificial ageing to temper T6. The microstructure of the alloys was characterised by optical and scanning electron microscopy and X-ray diffraction.

The main conclusions from this study are as follows:

- The increased constituent particle content led to a substantial reduction in the ductility for the tailor-made alloys compared with the engineering alloys in the cast and homogenised condition.
- Extrusion greatly improved the ductility of both the engineering and the tailor-made alloys, and the difference in ductility between them was markedly reduced. These improvements in ductility are mainly attributed to the breaking-up and redistribution of the constituent particles in the extrusion process.
- The notch sensitivity was substantial for all alloys, but only a small difference in notch sensitivity was found between the engineering alloys and the tailor-made alloys.
- In the cast and homogenised condition, the notch sensitivity was somewhat higher for the 6110 alloys than for the 6063 alloys, while after extrusion the 6110 alloys had considerably less notch sensitivity. The reason for the low notch sensitivity is attributed to the non-recrystallised grain structure of the 6110 alloys after extrusion.
- In the uniaxial tension tests, the extruded alloys exhibited weak or no significant anisotropy in the failure strain. The anisotropy in the failure strain was, however, stronger in the notch tension tests, where the ductility in most cases was higher in the extrusion direction.
- For the notched specimens of the extruded 6063 alloys, the higher content of constituent particles in the tailor-made alloy gave equal or slightly better ductility than for the engineering alloy. This finding was attributed to a lower propensity for intergranular fracture as suggested by the lower number of facets in the fracture surface.

Data availability

The raw/processed data required to reproduce the findings in the study cannot be shared at this time, as the data also forms part of several ongoing studies. However, the data may be made available from the corresponding author upon request.

CRediT authorship contribution statement

Asle Joachim Tomstad: Formal analysis, Investigation, Writing – original draft, Writing – review & editing, Visualization. **Susanne Thomesen:** Formal analysis, Investigation, Writing – original draft, Writing – review & editing. **Tore Børvik:** Conceptualization, Writing – original draft, Writing – review & editing, Supervision. **Odd Sture Hopperstad:** Conceptualization, Writing – original draft, Writing – review & editing, Supervision.

Declaration of competing interest

The authors declare that they have no known competing financial interests or personal relationships that could have appeared to influence the work reported in this paper.

Acknowledgments

The authors gratefully appreciate the financial support from NTNU and the Research Council of Norway through the FRINATEK Program FractAl, Project No. 250553.

References

[1] European aluminium, Vision 2050, https://www.european-aluminium.eu/media/2545/sample_vision-2050-low-carbon-strategy_20190401.pdf, 2019. (Accessed 22 February 2021).
[2] J.A.S. Green, Aluminum Recycling and Processing for Energy Conservation and Sustainability, ASM International, Materials park, USA, 2007.
[3] W. Khalifa, F.H. Samuel, J.E. Gruzleski, Iron Intermetallic phases in the Al corner of the Al-Si-Fe system, Metall. Mater. Trans. 34 (2003) 807–825.
[4] A.A. Benzerga, J.B. Leblond, Ductile fracture by void growth to coalescence, Adv. Appl. Mech. 44 (2010) 169–305.
[5] A. Pineau, A.A. Benzerga, T. Pardoen, Failure of metals I: brittle and ductile fracture, Acta Mater. 107 (2016) 424–483.
[6] F.M. Beremin, Cavity formation from inclusions in ductile fracture of A508 steel, Metallurgical Transactions A 12 (1981) 723–731.
[7] B.H. Frodal, K.O. Pedersen, T. Børvik, O.S. Hopperstad, Influence of pre-compression on the ductility of AA6xxx aluminium alloys, Int. J. Fract. 206 (2017) 131–149.
[8] H. Toda, H. Oogo, K. Horikawa, K. Uesugi, A. Takeuchi, Y. Suzuki, M. Nakazawa, Y. Aoki, M. Kobayashi, The true origin of ductile fracture in aluminum alloys, Metall. Mater. Trans. 45 (2014) 765–776.
[9] L. Babout, W. Ludwig, E. Maire, J.Y. Buffière, Damage assessment in metallic structural materials using high resolution synchrotron X-ray tomography, Nucl. Instrum. Methods Phys. Res. Sect. B Beam Interact. Mater. Atoms 200 (2003) 303–307.
[10] D. Lassance, D. Fabrègue, F. Delannay, T. Pardoen, Micromechanics of room and high temperature fracture in 6xxx Al alloys, Prog. Mater. Sci. 52 (2007) 62–129.
[11] M. Achouri, G. Germain, P. Dal Santo, D. Saidane, Experimental characterization and numerical modeling of micromechanical damage under different stress states, Mater. Des. 50 (2013) 207–222.
[12] H. Agarwal, A.M. Gokhale, S. Graham, M.F. Horstemeyer, Anisotropy of intermetallic cracking damage evolution in an Al-Mg-Si base wrought aluminium alloy under axial compression, Metall. Mater. Trans. 33 (2002) 3443–3448.
[13] H. Agarwal, A.M. Gokhale, S. Graham, M.F. Horstemeyer, Void growth in 6061-aluminum alloy under triaxial stress state, Mater. Sci. Eng., A 341 (2003) 35–42.
[14] J. Gurland, J. Plateau, The mechanism of ductile rupture of metals containing inclusions, Trans. ASM 56 (1963) 442–454.
[15] A. Weck, D.S. Wilkinson, E. Maire, Observation of void nucleation, growth and coalescence in a model metal matrix composite using X-ray tomography, Mater. Sci. Eng., A 488 (2008) 435–445.
[16] A.A. Benzerga, J. Besson, A. Pineau, Anisotropic ductile fracture: Part I: experiments, Acta Mater. 52 (2004) 4623–4638.
[17] A. Weck, D.S. Wilkinson, E. Maire, H. Toda, Visualization by X-ray tomography of void growth and coalescence leading to fracture in model materials, Acta Mater. 56 (2008) 2919–2928.
[18] T.B. Cox, J.R. Low, An investigation of the plastic fracture of AISI 4340 and 18 Nickel-200 grade maraging steels, Metallurgical Transactions 5 (1974) 1457–1470.
[19] A. Weck, D.S. Wilkinson, Experimental investigation of void coalescence in metallic sheets containing laser drilled holes, Acta Mater. 56 (2008) 1774–1784.
[20] F. Hannard, A. Simar, E. Maire, T. Pardoen, Quantitative assessment of the impact of second phase particle arrangement on damage and fracture anisotropy, Acta Mater. 148 (2018) 456–466.
[21] B. Kondori, T.F. Morgeneyer, L. Helfen, A.A. Benzerga, Void growth and coalescence in a magnesium alloy studied by synchrotron radiation laminography, Acta Mater. 155 (2018) 80–94.
[22] Y. Kato, K. Hisayuki, M. Sakaguchi, K. Higashi, Effect of alloy elements on microstructures and mechanical properties in Al-Mg-Si alloys, ICAA 13 (2012) 1521–1526. Pittsburgh.
[23] M.S. Remøe, K. Marthinsen, I. Westermann, K. Pedersen, J. Røyset, C. Marioara, The effect of alloying elements on the ductility of Al-Mg-Si alloys, Mater. Sci. Eng., A 693 (2017) 60–72.
[24] F. Hannard, S. Castin, E. Maire, R. Mokso, T. Pardoen, A. Simar, Ductilization of aluminium alloy 6056 by friction stir processing, Acta Mater. 130 (2017) 121–136.

[25] B.H. Frodal, E. Christiansen, O.R. Myhr, O.S. Hopperstad, The role of quench rate on the plastic flow and fracture of three aluminium alloys with different grain structure and texture, Int. J. Eng. Sci. 150 (2020) 103257.
[26] S. Thomesen, O.S. Hopperstad, O.R. Myhr, T. Børvik, Influence of stress state on plastic flow and ductile fracture of three 6000-series aluminium alloys, Mater. Sci. Eng., A 783 (2020) 139295.
[27] I. Westermann, K.O. Pedersen, T. Furu, T. Børvik, O.S. Hopperstad, Effects of particles and solutes on strength, work-hardening and ductile fracture of aluminium alloys, Mech. Mater. 79 (2014) 58–72.
[28] S. Thomesen, O.S. Hopperstad, T. Børvik, Anisotropic plasticity and fracture of three 6000-series aluminium alloys, Metals 11 (2021) 557.
[29] K. Marthinsen, J.M. Fridy, T.N. Rouns, K.B. Lippert, E. Nes, Characterization of 3-D particle distributions and effects on recrystallization kinetics and microstructure, Scripta Mater. 39 (1998) 1177–1183.
[30] O. Engler, V. Randle, Introduction to Texture Analysis: Macrotexture, Microtexture, and Orientation Mapping, second ed., CRC press, Taylor & Francis Group, 2010.
[31] M. Fourmeau, T. Børvik, A. Benallal, O.G. Lademo, O.S. Hopperstad, On the plastic anisotropy of an aluminium alloy and its influence on constrained multiaxial flow, Int. J. Plast. 27 (2011) 2005–2025.
[32] S. Thomesen, O.S. Hopperstad, T. Børvik, On the material characterization of an aluminium alloy using different specimens and identification methods, ICEM Proc. 2 (2018) 400.
[33] K.O. Pedersen, I. Westermann, T. Furu, T. Børvik, O.S. Hopperstad, Influence of microstructure on work-hardening and ductile fracture of aluminium alloys, Mater. Des. 70 (2015) 31–44.
[34] J. Aucote, D.W. Evans, Effects of excess silicon addition on ductility of Al- 0.95% Mg_2Si alloy, Met. Sci. 12 (1978) 57–63.
[35] D. Broek, The role of inclusions in ductile fracture and fracture toughness, Eng. Fract. Mech. 5 (1973) 55–66.
[36] G.T. Hahn, A.R. Rosenfield, Metallurgical factors affecting fracture toughness of aluminum alloys, Metallurgical Transactions A 6 (1975) 653–668.
[37] S. Thomesen, Plastic Flow and Fracture of Isotropic and Anisotropic 6000-series Aluminium Alloys: Experiments and Numerical Simulations, Ph.D. thesis. NTNU - Norwegian University of Science and Technology, Trondheim, Norway, 2019.
[38] C.I.A. Thomson, M.J. Worswick, A.K. Pilkey, D.J. Lloyd, Void coalescence within periodic clusters of particles, J. Mech. Phys. Solid. 51 (2003) 127–146.
[39] D. Steglich, W. Brocks, J. Heerens, T. Pardoen, Anisotropic ductile fracture of Al 2024 alloys, Eng. Fract. Mech. 75 (2008) 3692–3706.
[40] B.H. Frodal, D. Morin, T. Børvik, O.S. Hopperstad, On the effect of plastic anisotropy, strength and work hardening on the tensile ductility of aluminium alloys, Int. J. Solid Struct. 188–189 (2020) 118–132.
[41] T. Børvik, O.S. Hopperstad, T. Berstad, On the influence of stress triaxiality and strain rate on the behaviour of a structural steel. Part II. Numerical study, Eur. J. Mech. Solid. 22 (2003) 15–32.
[42] M. Alves, N. Jones, Influence of hydrostatic stress on failure of axisymmetric notched specimens, J. Mech. Phys. Solid. 47 (1999) 643–667.